Journal of Guidance, Control, and Dynamics
Vol. 48, No. 1, January 2025

Convolutional-Neural-Network-Based Autonomous Navigation of Hera Mission Around Didymos

Aurelio Kaluthantrige* and Jinglang Feng†
University of Strathclyde, Glasgow, Scotland G1 1XJ, United Kingdom
and
Jesús Gil-Fernández‡
European Space Agency, 2201 AZ Noordwijk, The Netherlands

https://doi.org/10.2514/1.G008054

The European Space Agency (ESA)'s Hera mission requires autonomous visual-based navigation in order to safely orbit around the target binary asteroid system Didymos and its moon Dimorphos in 2027. Nevertheless, the performance of optical-based navigation systems depends on the intrinsic properties of the image, such as high Sun phase angles, the presence of other bodies, and, especially, the irregular shape of the target. Therefore, to improve the navigation performance, thermal and/or range measurements from additional onboard instruments are usually needed to complement optical measurements. However, this work addresses these challenges by developing a fully visual-based autonomous navigation system using a convolutional-neural-network (CNN)-based image processing (IP) algorithm and applying it to the detailed characterization phase of the proximity operation of the mission. The images taken by the onboard camera are processed by the CNN-based IP algorithm that estimates the position of the geometrical centers of Didymos and Dimorphos, the range from Didymos, and the associated covariances. The results show that the developed algorithm can be used for a fully visual-based navigation for the position of the Hera spacecraft around the target with good robustness and accuracy.

Nomenclature

AE	=	absolute error
COM	=	center of mass
f	=	focal length
P	=	covariance matrix of the state
PE	=	percent error
Q	=	covariance matrix of the process
R	=	covariance matrix of the measurement
v	=	velocity
ν	=	pixel size
ρ	=	range
σ	=	standard deviation

I. Introduction

SMALL celestial bodies are remnants of the ancient solar system, holding invaluable insights into its evolutionary history. Asteroids and comets have garnered attention as prime targets for numerous space missions in the past years, such as Hayabusa 1 and 2, exploring asteroid Itokawa; Rosetta, a comet rendezvous mission targeting Comet 67P/Churyumov-Gerasimenko; and OSIRIS-REx, which sampled asteroid Bennu [1–4]. The European Space Agency (ESA) contributes to small bodies' exploration with Hera, a planetary defense mission under development in their Space Safety and Security Program. The Hera mission represents the European contribution to the international collaboration Asteroid Impact and Deflection Assessment (AIDA) with NASA. The main purpose of AIDA is to demonstrate the deflection of a hazardous asteroid by means of kinetic impact. The Double Asteroid Redirection Test (DART) spacecraft is the kinetic impactor designed by NASA, which performed successfully the impact on the 26th of September 2022. The Hera mission will rendezvous in early 2027 with the target asteroid and characterize its physical and dynamic properties, including the crater made by the impactor and the momentum transfer efficiency [5,6]. Furthermore, Hera aims to bring clarity to the currently uncertain mass measurements of the asteroid, and it will delve into the possible presence of recently deposited material, which could potentially constitute reaccreted ejecta following the impact of DART.

The destination of Hera is (65803) Didymos, a binary asteroid consisting of the primary Didymos and its moon Dimorphos, objective of DART's impact. Table 1 shows the relevant characteristics of the binary asteroid system, provided by the Didymos Reference Model document and updated with the Design Reference Asteroid document that reports data collected with the DART mission [7,8]. Accompanying Hera on this mission are two CubeSats: Milani and Juventas. While Milani is tasked with capturing detailed imagery of the DART crater, Juventas will conduct comprehensive assessments of Dimorphos' internal structure [9].

Following the interplanetary cruise phase, Hera will perform a series of ΔVs in order to reduce the relative velocity of the spacecraft with respect to the target, which marks the beginning of the proximity operations. The focus of this research is on the early characterization phase (ECP) and the detailed characterization phase (DCP) designed to achieve physical and dynamic characterizations of the binary asteroid [10]. Specifically, the characterization is aimed to improve the accuracy of the values shown in Table 1, together with other parameters related to the binary system, such as the rotation rate of both bodies, the geometric albedo, mass properties, and the gravitational field.

To ensure a high level of autonomy, the spacecraft is equipped with onboard instruments to accurately determine its position relative to the asteroid system. To meet this requirement, a vision-based navigation system is implemented in the guidance, navigation, and control (GNC) system of the spacecraft, which incorporates an onboard camera, image processing (IP) algorithms, and a navigation filter. The HERA GNC baseline incorporates a hyperspectral/thermal camera and a laser altimeter called planet altimeter (PALT). These additional instruments enhance the navigation strategy's reliability: the hyperspectral/thermal imager helps to overcome limitations caused by shadows and Sun phase angle issues, while PALT improves

Previously presented as Paper 22-720 at the 2022 AAS/AISS Astrodynamics Specialist Conference, Charlotte, NC, August 7–11, 2022; received 1 November 2023; accepted for publication 30 July 2024; published online 11 October 2024.

*Ph.D. Student, Department of Mechanical and Aerospace Engineering, 75 Montrose Street; mewantha.kaluthantrige-don@strath.ac.uk.

†Lecturer, Department of Mechanical and Aerospace Engineering, 75 Montrose Street; jinglang.feng@strath.ac.uk.

‡Guidance, Navigation and Control Engineer, European Space Research and Technology Centre, Keplerlaan 1; jesus.gil.fernandez@esa.int.

Table 1 Didymos' characteristics [7,8]

Parameter	Didymos	Dimorphos
Gravitational parameter, km^3/s^2	$3.5 \cdot 10^{-8}$	$2 \cdot 10^{-10}$
Extent along principal axis x, m	849	177
Extent along principal axis y, m	851	174
Extent along principal axis z, m	620	116

estimations in the radial direction, which are typically challenging for a vision-based GNC system. The camera employed in this system is the asteroid framing camera (AFC) [11].

Each day during the proximity operations is divided into two operational segments: data acquisition and data transmission. Within a single operational day, one set of each is scheduled in the following sequence: 15.5 hr for acquisition and 8.5 hr for transmission. For the ECP and the DCP, an autonomous attitude navigation is designed, which relies on an IP algorithm that estimates the pixel position of the center of mass (COM) of the main body in the images. Subsequently, the algorithm estimates the line of sight (LOS) of the spacecraft [11,12]. During the ECP, the performance of the autonomous attitude navigation system is rehearsed while the spacecraft is flying at a safer distance from the target. Data gathered during the ECP are transmitted to ground within the time interval of data transmission in order to update, if necessary, the IP algorithm. Once the system is verified, the system can be used during the DCP [13].

Despite the validation process, standard IP algorithms are strongly influenced by the inherent characteristics of the taken images. Elements such as the overall noise, lighting status, the appearance of secondary or undesired objects, and the irregular shape of the target can all impact the accuracy of the optical measurements [14–16]. While the GNC system of the Hera mission tackles these IP challenges by relying on the additional onboard instruments, the authors of this work addressed them with a convolutional-neural-network (CNN)-based IP algorithm built and presented in [17]. The algorithm is able to estimate accurately from the images captured by the AFC the position of the centroids of Didymos and Dimorphos and the range from the primary during the ECP and the DCP trajectories. The reader is referred to that work for a comprehensive understanding of the pipeline undertaken for the development of such an algorithm. Nevertheless, the work is performed with the pre-impact shape models of Didymos and Dimorphos.

In this work, we build upon the CNN-based IP algorithm to develop a fully autonomous visual-based navigation algorithm for the DCP trajectory of the Hera mission around the target body Didymos. We leverage the previous phase of the mission, the ECP, to train the CNN-based IP algorithm with a dataset of images representing the new shape of the targets Didymos and Dimorphos. The algorithm is expanded by providing the covariance matrix associated with each measurement and a flag that informs the filter whether the centroid of Dimorphos is visible or not, which is a unique contribution of this work. An unscented Kalman filter (UKF) combines the measurements obtained by the CNN-based IP algorithm with the information retrieved from the dynamic environment to provide the optimal estimate of the relative position of the spacecraft with respect to Didymos. In addition, the developed navigation algorithm relies fully on the AFC without requiring the inputs of the hyperspectral/thermal imager and PALT. Another contribution of this work is the utilization of the position of the centroid of Dimorphos for navigation.

The organization of this paper is as follows: Section II reviews the state-of-the-art of navigation systems around smaller bodies. Section III describes more in detail the proposed IP algorithm and the navigation filter. In Sec. IV, we conduct the numerical simulations and discuss the results. Section V, in conclusion, summarizes this research and suggests prospective areas for future work.

II. Related Methods

This section gives a review of the navigation strategies adopted by previous missions that successfully approached small solar system bodies.

A. Heritage Missions

1. *Rosetta*

In July 2014, the ESA interplanetary spacecraft Rosetta conducted a rendezvous with the comet 67P/Chuyumov-Gerasimenko. At 130 km of distance with respect to the target, Rosetta navigated toward the target, relying on optical measurements provided by the onboard navigation camera NAVCAM. The strategy consisted in matching the newly acquired images with a database of old images for which the geometry is known, using small-scale three-dimensional high-resolution maps (maplets) built around visible landmarks of the target body. The maplets consist of a height and an albedo map built on-ground with the available shape model of the target [18].

2. *Hayabusa 1 and 2*

Hayabusa 1 spacecraft performed approaching and landing on the target asteroid Itokawa in November 2005. To maintain the relative position to the asteroid during proximity operations, a visual-based GNC system was developed, similar to that of the Hera mission. Two wide-angle cameras, an IP algorithm estimating the position of the centroid of the target, and a light detection and ranging (LIDAR) estimating the range from the target have been used.

Hayabusa 2 spacecraft approached the target asteroid Ryugu in July 2018. As its predecessor, Hayabusa 1, this spacecraft is also provided with two wide-angle cameras and a LIDAR. Both spacecraft had on board a thermal infrared imager and a near-infrared camera spectrometer for scientific purposes but also to increase the robustness of the navigation system as for the Hera mission [19,20].

3. *OSIRIS-REx*

OSIRIS-REx used two wide-range cameras of the camera suite OCAMS (OSIRIS-REx Camera Suite) and the touch-and-go camera system TAGCAMS (Touch And Go Camera System) for the proximity operations navigation around the target asteroid Bennu. Stereo-photoclinometry was used to create digital terrain maps for landmark tracking technique, while the onboard LIDAR solves for the radial direction estimation [21].

4. *DART*

DART utilized the Small-body Maneuvering Autonomous Real-Time Navigation (SMART Nav) algorithm in conjunction with images obtained from the onboard Didymos Reconnaissance and Asteroid Camera for Optical Navigation (DRACO) to carry out autonomous terminal navigation in order to target the center of brightness (COB) of Dimorphos. The onboard ephemeris was updated with optical navigation data collected by DRACO till about 4 hr before the impact, after which the spacecraft went fully autonomous with SMART Nav [22].

B. Summary

The navigation techniques involved in Rosetta and OSIRIS-REx have in common the usage of asteroid models to be rendered for correlation with real images acquired with the onboard cameras. Therefore, prior knowledge of the surface appearance of Didymos would be required to employ these navigation strategies. Furthermore, the more complex the model, the more computationally expensive it is to run the technique onboard. To apply DART's SMART Nav algorithm, constant direct communication with ground is necessary for the real-time updating of the ephemeris, which is not the case of Hera, which alternates its attitude for data acquisition and transmission. Finally, the optical navigation solutions employed by Hayabusa 1 and 2 are similar to Hera and, as such, rely on multiple instruments to improve the robustness, while the purpose of this work is to provide a navigation strategy with good robustness that relies only on the images captured by the onboard camera.

III. Methodology

This section provides a detailed description of the methodology applied in this work. A terminology is briefly clarified to streamline the discussion. In this work, centroid or COM are referred to the body's geometrical center projected on the image. While this assumption is almost valid for Didymos given its ellipsoidal shape, it is not certain if it holds true for Dimorphos consequently to the DART impact that may have modified its shape [23]. Figure 1 shows the main steps of the overall pipeline. Given a reference trajectory, at epoch t_{k+1}, a new image is captured by the onboard AFC. In this work, synthetic images generated with the software Planet and Asteroid Natural Scene Generation Utility (PANGU) are used. The image is input to the IP block, and it goes several steps detailed in Sec. III.C in order to provide four different estimations: the position of the centroid of Didymos, the range from Didymos, the centroid of Dimorphos (if available), and the associated covariance matrix for each measurement. The IP consists firstly in a preprocessing step, where the image undergoes an initial normalization before it is handled by the CNN aimed to regress specific keypoints on the image. The CNN outputs a sequence of heatmaps, each one associated with the regressed keypoint. The postprocessing block analyzes the heatmaps and outputs the position of the keypoints and the intensities of the heatmaps. The latter are used to calculate the covariance matrices and to inform whether an estimate of Dimorphos' centroid position is available with a Boolean variable represented by Flag Dimorphos. Finally, an UKF combines the available measurements and the propagated state to provide the best estimate for the state of the spacecraft at epoch t_{k+1}.

This work is an extension of [17], where the main focus was to build an IP algorithm supported by CNNs able to provide optical measurements for the navigation of Hera using the pre-impact shape models of Didymos and Dimorphos. In contrast, this research is focused on refining the previous algorithm with the latest shape models and combining it with an UKF in order to solve for the state estimation of the Hera spacecraft. We use the same reference trajectories (Sec. III.A), software to generate the database of images (Sec. III.B), CNN architecture (Sec. III.C.2), and centroiding and range estimation methodologies (Sec. III.D). The subsequent part of this section contains a thorough explanation of the applied methodology.

A. Reference Trajectories

The reference trajectories used in this work are represented in the target body equatorial inertial (TB) reference frame, which has the geometrical center of Didymos as the origin of the axes, the X axis pointing as the Earth-centered ecliptic inertial, and the XY plane lying in the same plane as the equator of Didymos. A summary of the most relevant information about the orbit of the binary system is reported in Table 2 [24,25]. The orbit of Dimorphos considered in this work is before the DART impact. The reference trajectories employed in this work are from the ECP and the DCP proximity operations. The former is used to train the CNN and to tune the parameters of the postprocessing, while the latter is used as a test case scenario.

Table 2 Selected orbital properties of Didymos system [24,25]

Parameter	Value
Heliocentric orbit	
Semimajor axis, AU	1.642665 ± 2.7214e − 9
Eccentricity	0.383264 ± 1.3374e − 10
Inclination, °	3.41415 ± 1.6188e − 8
Longitude of ascending node, °	72.987867 ± 2.1852e − 7
Orbital period, yr	2.105386 ± 5.2320e − 10
Binary orbit	
Semimajor axis, m	1190 ± 30
Eccentricity	0
Orbital period, hr	11.93 ± 0.01

The ECP trajectory is provided by ESA, while the DCP trajectory is provided by GMV Aerospace and Defence, in charge of the GNC simulator of the Hera mission. Both trajectories consist of hyperbolic arcs; the spacecraft cannot be placed into captured orbits due to the limited prior knowledge of Didymos' dynamic environment. The arcs are designed so that the AFC, whose parameters are shown in Table 3, is able to contain within its field of view (FOV) the whole shape of Didymos in a single image in order to use the centroiding algorithm [13,26,27].

Figure 2 depicts the spacecraft's ECP trajectory along with the relative position of the sun (reduced in size in the visual representation) and Dimorphos' orbit. The trajectory is composed of four arcs, with the initial epoch set at $t_{\text{in}} = 9012$ days and the final epoch at $t_{\text{fin}} = 9026$ days calculated in the Modified Julian Date 2000 (MJD2000). The second and the fourth arcs are 3 days long and go, respectively, from Didymos' high latitudes to low latitudes and

Table 3 AFC properties [26,27]

Parameter	Value
FOV	5.5°
Focal length (f)	10.6 cm
Aperture	2.5 cm
Image size	1024 × 1024 pxl
Pixel size (ν)	14 μm

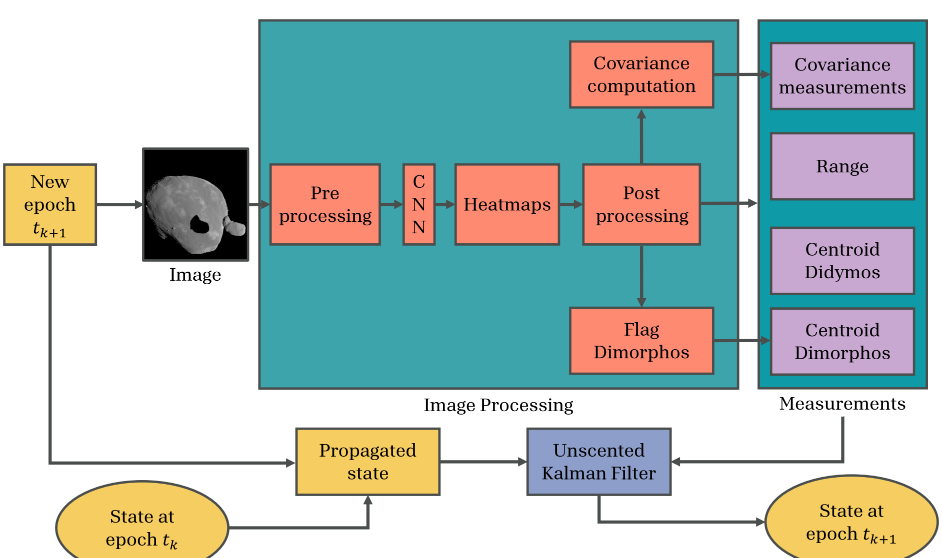

Fig. 1 Overall visual-based navigation algorithm.

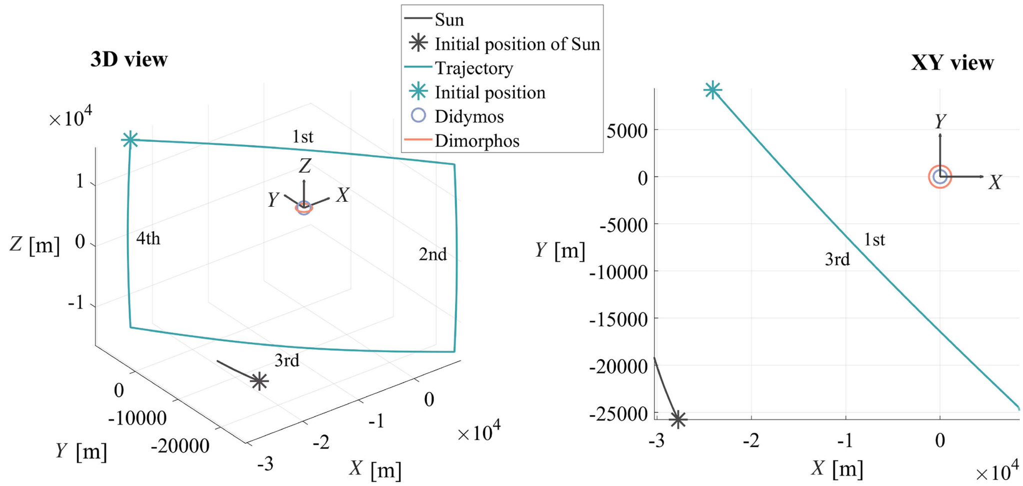

Fig. 2 ECP trajectory.

vice versa. The first and the third arcs are 4 days long and cover the poles of the target. The sole gravitational forces from the point masses of both bodies and the orbital maneuvers at the joint of two arcs are taken into account. The planar view illustrated in Fig. 2 shows that the ECP trajectory is placed between the Sun and Didymos in order to provide the AFC with visible images of the target [10]. Figure 3 shows that the distance from the primary ranges from 20 to 30 km.

Figure 4 depicts the spacecraft's DCP trajectory along with the relative position of the sun (reduced in size in the visual representation) and Dimorphos' orbit. The trajectory is composed of eight Z-shaped arcs located between the target and the Sun's position, with a total duration of 28 days, plus 3 days of transition from the ECP. The distance from the primary ranges approximately from 9 to 23 km, as illustrated in Fig. 5. The minimum distance is established to guarantee that the complete shape of Didymos remains within the FOV of the AFC, even when there is a navigation error of up to 100 m. In the actual mission, the ECP and the DCP last 4 weeks each, but in this work the whole DCP and only half of the ECP are considered, as provided by ESA and GMV Aerospace and Defence.

B. Image Generation

Software PANGU is used to generate the database of synthetic images for this work. PANGU is a simulation tool developed by the

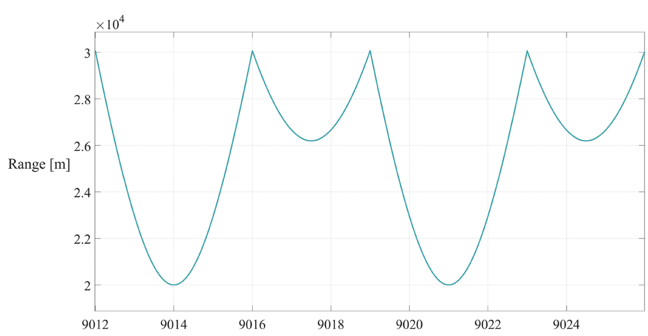

Fig. 3 Range from Didymos during ECP trajectory.

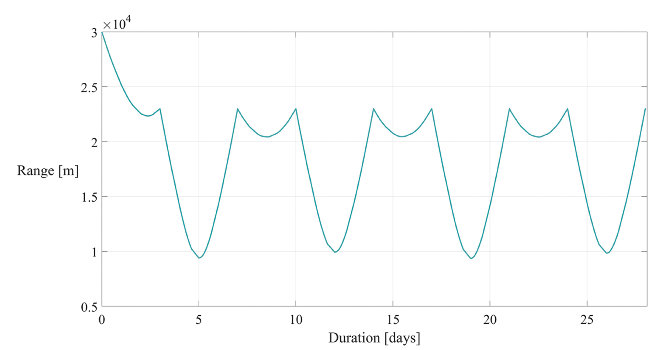

Fig. 5 Range from Didymos during DCP trajectory.

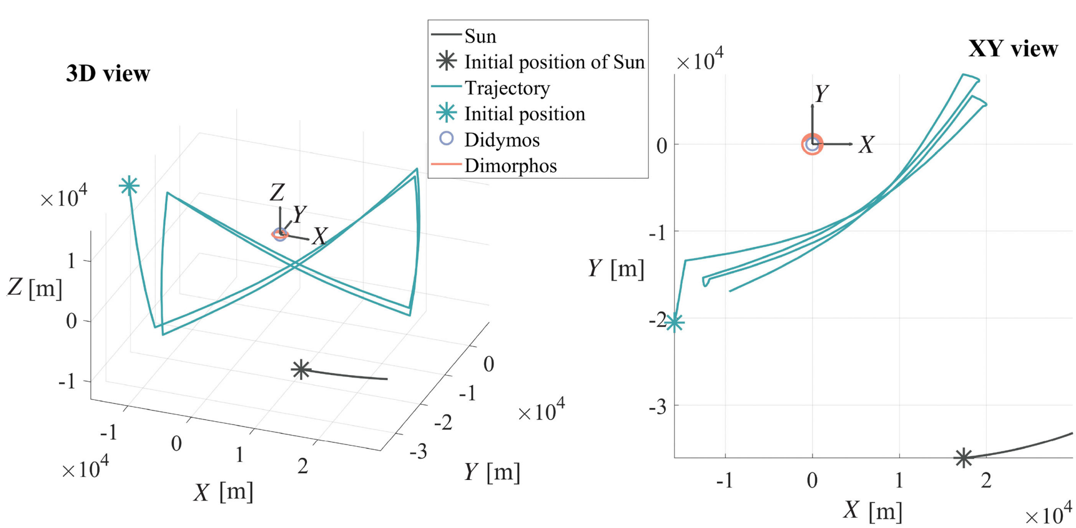

Fig. 4 DCP trajectory.

STAR-Dundee engineering company, and it is capable of modeling planetary and asteroid surfaces and providing high-fidelity visualizations of images in near real-time [28]. The shape models of Didymos and Dimorphos are provided by GMV and updated with the data collected with the DART mission shown in Table 1. Didymos' shape is ellipsoidal, with the extent along its x and y axes larger than the extent along its z axis, as shown in Table 1. Dimorphos' shape before DART's impact was an oblate ellipsoid, which is approximated in this work scaling down the shape model of asteroid Itokawa.

PANGU generates grayscale images as seen from the AFC with the properties shown in Table 3 and displays them on its viewer with its coordinate frame's origin at the top left corner and the horizontal and vertical axes referred to as i direction and j direction, respectively, as illustrated in the example of Fig. 6.

For asteroid imaging during the ECP and DCP trajectories, the AFC's boresight is aligned with Didymos' position vector, and the camera's vertical axis is orthogonal to the spacecraft–Sun's position vector to the spacecraft [10], which results in images displayed on the viewer consistently portraying the target illuminated from the right side.

In this work, PANGU is used to generate the following:

1) Dataset 1: 40,000 images generated during the ECP trajectory and used for the training and validation of the CNN and to tune the parameters of the IP algorithm. Two fictitious additional arcs are considered, the first arc connecting the end of the second arc with the beginning of the first one, and the second one connecting the end of the third arc with the end of the first one, as shown in Fig. 7. The augmented ECP trajectory is sampled randomly to generate a secondary trajectory closer to the target, with a minimum distance of 7 km, in order to train and validate the IP algorithm, with a pool of images showing the asteroid in multiple configurations relative to the spacecraft. A pointing error of the AFC boresight direction with values spanning between $[-0.3, 0.3]°$ is considered for each image to randomize the position of the projected centroid of Didymos on the image plane.

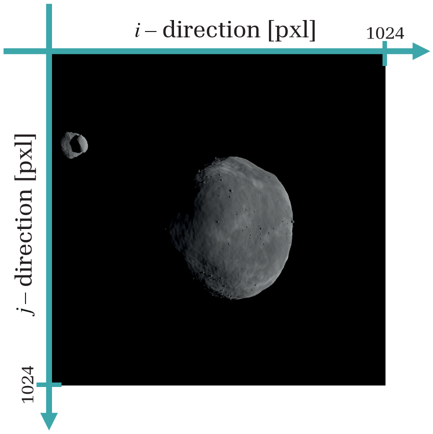

Fig. 6 Image taken during the ECP trajectory shown on the PANGU viewer.

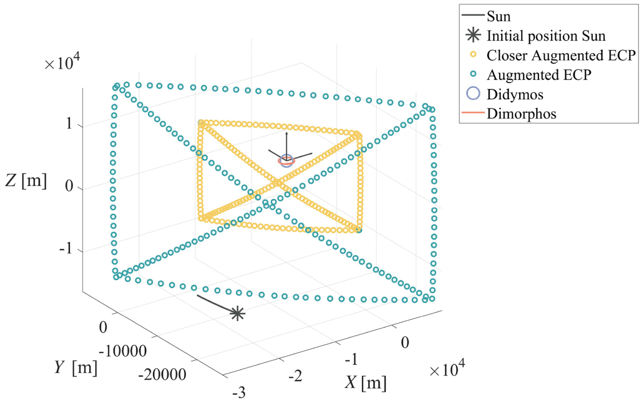

Fig. 7 Augmented ECP trajectory.

2) Dataset 2: 450 images taken sampling the DCP trajectory every 3600 s and used as testing batch for the whole visual-based navigation pipeline. A pointing error of the AFC boresight direction with values spanning between $[-0.5, 0.5]°$ is considered for each image to randomize the position of the projected centroid of Didymos on the image plane.

The pointing error values considered in the generation of the images of Dataset 1 and Dataset 2 are chosen taking into account the only mission requirement of having the whole shape of Didymos within the FOV of the camera [10].

C. Image Processing

In this section, the operations that each image undergoes with the IP algorithm are described, as represented in Fig. 8.

1. *Normalization*

Once an image is generated with PANGU, its size is reduced from 1024×1024 pxl to 256×256 pxl, and consequently it is normalized using Eq. (1) to calibrate the different pixel intensities, which helps the CNN to converge faster for a given learning rate. Equation (1) shows that the image is converted from grayscale to RGB as required by the specific CNN architecture chosen in this work.

$$\text{Image} = \text{Image} - \text{Mean}/\text{Std} \tag{1}$$

where Mean $= [0.485, 0.456, 0.406]$ and Std $= [0.229, 0.224, 0.225]$. Figure 8 shows the output normalized image of the preprocessing block (the colors of the output image are enhanced for visualization purposes).

2. *Convolutional Neural Network*

The CNN employed in this work is the High-Resolution Network (HRNet), the state-of-the-art CNN architecture for keypoints regression, with its ability to maintain high-resolution representation of the input image through the whole net [29]. The keypoints to regress for each synthetic image are 26, and they are the COM of Didymos, COM_{Did}, the COM of Dimorphos, COM_{Dim}, and 24 points on the visible limb, i.e., the right side, segmenting Didymos from the background. The positions of the 24 points are used together with the position of the COM_{Did} to estimate the range from Didymos, as it is explained in Sec. III.D. The reader is referred to [17] for the methodology applied to retrieve the ground truth (GT) positions of the 26 keypoints on the images.

In this work, we utilize the CNN architecture known as pose-hrnet-w32 [30]. Throughout the training process, the validation dataset is employed alongside the training dataset to calculate validation losses, thereby preventing overfitting. For training and validation, Dataset 1 is not used entirely, as images where Dimorphos is located outside of the image plane or behind Didymos are discarded. Whether Dimorphos is visible or not in the testing dataset is handled by the postprocessing block of the IP. Consequently, the training and validation datasets consist, respectively, of 15,156 (93.73%) images and 520 (3.22%) images from Dataset 1, while the testing dataset consists of the whole 450 (3.05%) images from Dataset 2. The training utilizes the Adam optimizer, employing a learning rate that follows a cosine decay schedule, initialized at 10^{-3} and decaying at a rate of 0.1. The overall number of parameters engaged in the training process amounts to 28,536,410.

The CNN model undergoes training for 210 epochs, which approximately equates to 48 hr of training time. This training is conducted on a virtual machine hosted by Google Colab, utilizing the NVIDIA V100 Tensor Core GPU. The trained model is then converted into an Open Neural Network Exchange (ONNX) open format and imported on MATLAB. The trained HRNet with the updated weights and biases has an overall weight of 109 MB.

The outputs of the HRNet consist in a sequence of heatmaps of size 64×64 pxl, each one associated with the corresponding keypoint. A heatmap is a cloud of white pixels around the estimated keypoint, and it represents the estimated accuracy in regressing the position of that particular keypoint. The smaller and more intense the heatmap, the more accurate is the estimation of the position of the associated

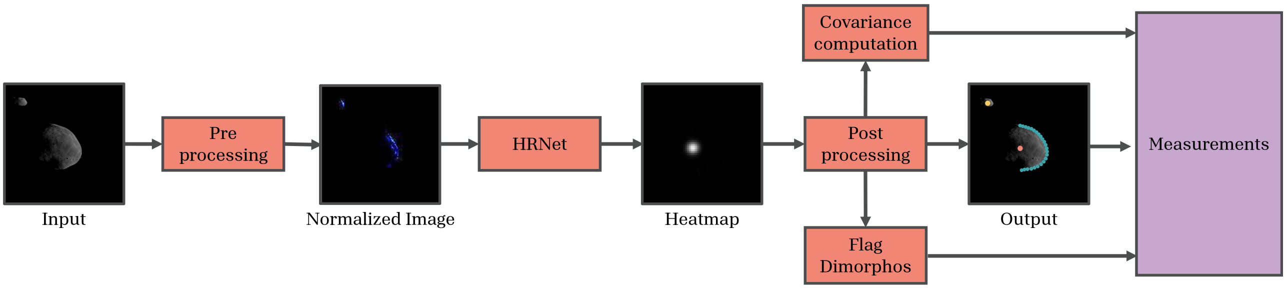

Fig. 8 Image processing.

keypoint. Figure 9 shows an example of the heatmap around the estimated position of the COM of Didymos.

3. Postprocessing

In the postprocessing block, the 26 heatmaps associated with each keypoint are analyzed. Specifically, the postprocessing block has three main functions:

1) To remove the white noise by thresholding each heatmap image so that the only nonblack pixels are the ones associated with the heatmap

2) To extract the peak intensity of the heatmap and its x and y coordinates

3) To obtain a statistical population around the heatmap's peak

The coordinates of the points with the peak pixel intensity within the heatmap define the estimated position of the regressed 26 keypoints. The intensity and shape of the heatmap convey the level of confidence in accurately pinpointing the associated keypoint at that particular position. Therefore, in this work, the statistical population around the regressed keypoint is used to derive the associated covariance matrix.

4. Flag Dimorphos

By analyzing the peak intensity of the heatmaps associated with the COM of Dimorphos and generated by the trained HRNet with the entire Dataset 1, it is derived a threshold value to determine whether Dimorphos is visible or not. Figure 10 shows the mentioned peak intensities, together with their average value and the cutoff threshold value. Three main regions of peak intensities are identified:

1) 0–0.3: Heatmaps' peak intensities associated to images where Dimorphos is hardly visible or not visible

2) 0.3–0.782649: Heatmaps' peak intensities associated to images where Dimorphos is in eclipse or is partially visible

3) >0.782649: Heatmaps' peak intensities associated to images where Dimorphos is fully visible

Figure 11 shows three sample images of each region, along with the heatmaps associated with the regression of the centroids of both bodies. The output of this block is a Boolean variable that is true if the peak intensity of Dimorphos' centroid heatmap is higher than 0.3, i.e., Dimorphos is at least partially visible or in eclipse.

5. Covariance Computation

In this block of the IP algorithm, the covariance matrices associated with the error in the estimation of the position of the centroids of Didymos and Dimorphos are computed. Given the x_i and y_i coordinates of the ith pixel belonging to the heatmap associated to the regressed centroid of coordinates x_p and y_p, the covariance of the error is calculated with Eqs. (2) and (3), in accordance with [31].

$$P_{\text{COM}} = \begin{pmatrix} \text{cov}(x,x) & \text{cov}(x,y) \\ \text{cov}(y,x) & \text{cov}(y,y) \end{pmatrix} \tag{2}$$

$$\text{cov}(x,y) = \sum_{i=1}^{n} w_i (x_i - x_p) \cdot (y_i - y_p) \tag{3}$$

where n is the number of pixels in each keypoint's heatmap and w_i is a weight that takes into account the intensity of the pixel belonging to the heatmap. This process aims to assign greater weight to pixels that exhibit high brightness and are situated near the peak, while assigning reduced importance to pixels with low intensity that are distant from the peak. Figure 12 shows two examples of covariance matrices associated with the estimation of the centroids of both bodies. The example on the image of the right of Fig. 12 shows that Dimorphos' centroid estimation covariance can reach lower values than the one of Didymos due to its relative reduced size on the image. Therefore, the cloud of points associated with Dimorphos' centroid estimation is smaller. In order to account for the different sizes of the bodies, a tuning of the covariance is applied accordingly. The tuning consists in adjusting the parameters of the covariance matrices to weigh majorly the estimation of the centroid of Didymos with respect to the one of Dimorphos.

D. Measurements

The input measurements of the navigation filter are the estimated position of the centroids of Didymos and Dimorphos (when available) and the estimated range from Didymos. The first two are direct outputs of the IP block together with their associated covariance matrices. The range is estimated using the relative average distance in pixels (n_R) of the 24 regressed keypoints on the visible limb of

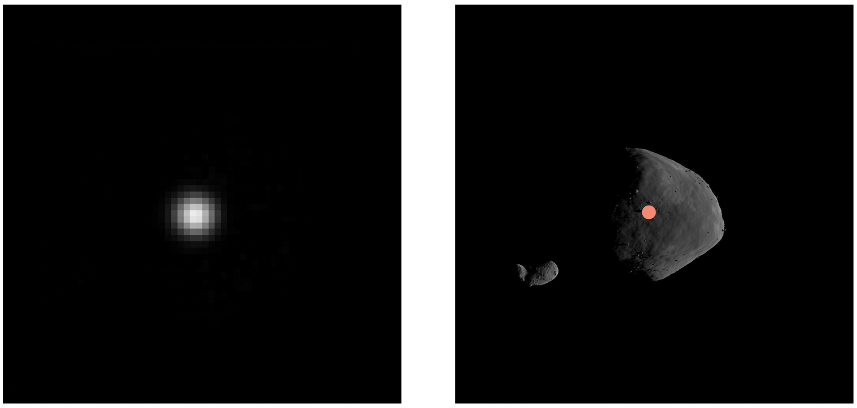

Fig. 9 Heatmap associated to the position of the centroid of Didymos.

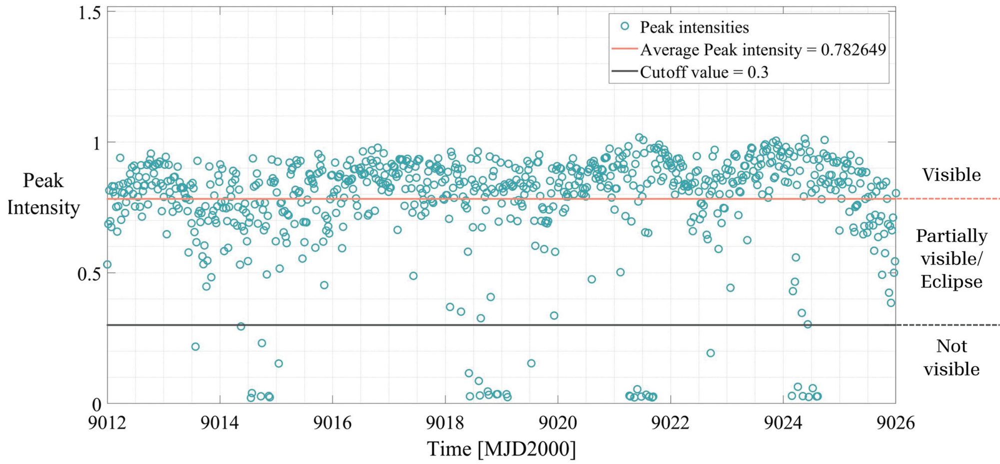

Fig. 10 Peak intensity of the heatmaps associated to $\mathrm{COM_{Dim}}$ generated with dataset 1.

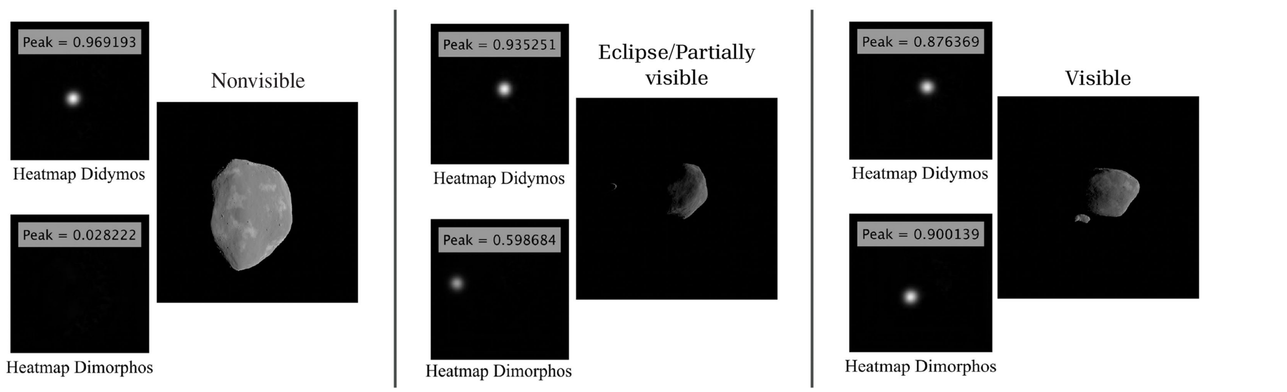

Fig. 11 Heatmaps of $\mathrm{COM_{Did}}$ and $\mathrm{COM_{Dim}}$ associated with three sample images showing Dimorphos, respectively, nonvisible, in eclipse, and visible.

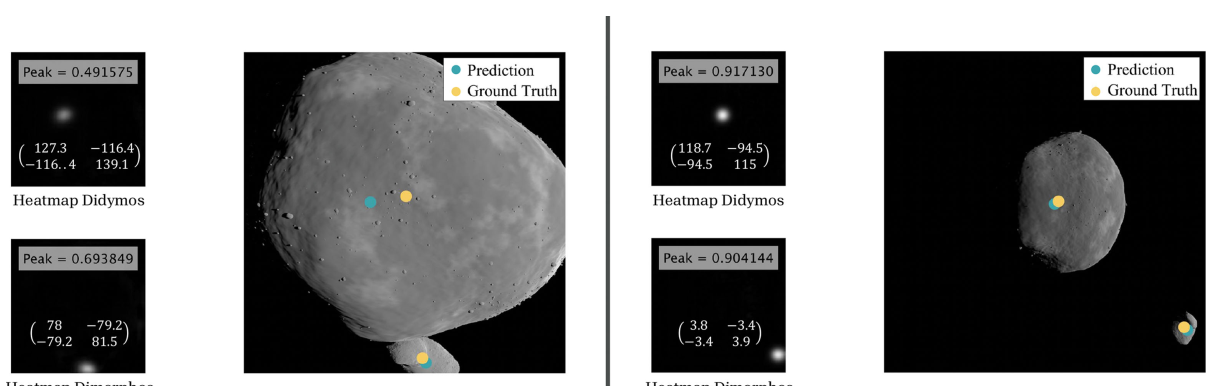

Fig. 12 Two examples of covariance matrices associated with the centroids of Didymos and Dimorphos.

Didymos with respect to its estimated COM, as explained in [17]. The 24 keypoints have an equal relative angular distance and span an angular aperture of $[-87, 87]^\circ$ with respect to the i direction of the PANGU viewer. By applying the pinhole camera model using the properties of the AFC shown in Table 3 and by approximating the shape of Didymos as a sphere of diameter $D = 773.33$ m (average value of the extent along the three principal axis shown in Table 1), the range ρ is estimated, as shown in Eq. (4):

$$\rho = \frac{f \cdot D}{n_R \cdot \nu} \tag{4}$$

where f is the focal length and ν is the pixel density, as shown in Table 3. The covariance of the error associated with the estimated range is obtained by applying Eq. (4) to Dataset 1 and by comparing it with the range's GT value. The error obtained is reported on Table 4, and the covariance of the error chosen in this work is $P\rho = \mathrm{MAE}^2$.

Table 4 Range estimation error for dataset 1

Parameter	Value
Mean absolute error (MAE), m	854.9
σ_{MAE}, m	518.85
Mean absolute percent error (MAPE), %	5.68
σ_{MRAE}, %	4.3

The absolute error (AE) and the absolute percent error (APE) are defined as follows:

$$\mathrm{AE} = |\mathrm{Range}_{\mathrm{est}} - \mathrm{Range}_{\mathrm{GT}}| \tag{5}$$

$$\mathrm{APE} = \frac{|\mathrm{Range}_{\mathrm{est}} - \mathrm{Range}_{\mathrm{GT}}|}{\mathrm{Range}_{\mathrm{GT}}} \cdot 100\% \tag{6}$$

E. Navigation Filter

To combine the measurements produced by the IP algorithm with the dynamic environment and form an accurate estimate of the state of the spacecraft, a navigation filter is implemented. The relative state of the spacecraft with respect to Didymos to be estimated consists of the three coordinates of the relative position and the three coordinates of the relative velocity. The measurements are available for each image of Dataset 2, therefore every 3600 s.

The UKF is based on a nonlinear uncertainty propagation technique called the unscented transform (UT) that captures the propagation of the statistical properties of state estimates through nonlinear functions. This is done using a set of sigma points that are built with the matrix square root of the covariance matrix of the state. Assume the following n-state discrete-time nonlinear system x with measurement equation z [32]:

$$\begin{aligned} x_{k+1} &= f(x_k) + w_k, \\ z_k &= h(x_k) + v_k, \\ w_k &\sim (0, Q_k), \\ v_k &\sim (0, R_k) \end{aligned}$$

where f is a nonlinear state transition function from discrete time k to $k+1$, and w and v are, respectively, the process and measurement noise. The individual steps of the UKF are shown in Algorithm 1. W_n^i and W_c^i are weights that determine the spread and the distribution of the sigma points around the mean state value, while c is a scaling factor based on the size of the state.

Algorithm 1: Unscented Kalman Filter

Initialize:
$\hat{x}_0 = \mathbb{E}[x_0]$
$P_0 = \mathbb{E}[(x_0 - \hat{x}_0) \cdot (x_0 - \hat{x}_0)^T]$
for Each measurement z_k at epoch $k = 1, \ldots, t_f$ **do**
Calculate sigma points and the associated predicted measurements:
$\hat{x}^{(0)}_{k|k-1} = \hat{x}_{k|k-1}$
$\Delta x^{(i)} = \left(\sqrt{cP_{k|k-1}}\right)_i$ for $i = 1, \ldots, n$
$\Delta x^{(n+i)} = -\left(\sqrt{cP_{k|k-1}}\right)_i$ for $i = 1, \ldots, n$
$\hat{x}^{(i)}_{k|k-1} = \hat{x}_{k|k-1} + \Delta x^{(i)}$ for $i = 1, \ldots, 2n$
$\hat{z}^{(i)}_{k|k-1} = h\left(\hat{x}^{(i)}_{k|k-1}\right)$ for $i = 1, \ldots, 2n$
Combine the predicted measurements of each sigma point to obtain the mean predicted measurement at time k:
$\hat{z}_k = \sum_{i=0}^{2n} W_n^{(i)} \hat{y}^i_{k|k-1}$
Estimate the covariance of the predicted measurement:
$P_{zz} = \sum_{i=0}^{2n} W_c^{(i)} (\hat{z}^{(i)}_{k|k-1} - \hat{z}_k) \cdot (\hat{z}^{(i)}_{k|k-1} - \hat{z}_k)^T + R_k$
Estimate the cross-covariance:
$P_{xz} = \sum_{i=0}^{2n} W_c^{(i)} (\hat{x}^{(i)}_{k|k-1} - \hat{x}_{k|k-1}) \cdot (\hat{z}^{(i)}_{k|k-1} - \hat{z}_k)^T$
Update Step:
$K_k = P_{xz} P_{zz}^{-1}$
$\hat{x}_{k|k} = \hat{x}_{k|k-1} + K(z_k - \hat{z}_k)$
$P_{k|k} = P_{k|k-1} - K_k P_{zz} K_k^T$
Prediction Step:
Calculate the sigma points and propagate with function f:
$\hat{x}^{(i)}_{k|k+1} = f(\hat{x}^{(i)}_{k|k})$
Combine the predicted state for each sigma point to compute the mean predicted state at epoch $k+1$:
$\hat{x}_{k+1|k} = \sum_{i=0}^{2n} W_n^{(i)} \hat{x}^i_{k+1|k}$
Compute the covariance of the predicted state at epoch $k+1$:
$P_{k+1|k} = \sum_{i=0}^{2n} W_c^{(i)} (\hat{x}^{(i)}_{k+1|k} - \hat{x}_{k+1|k}) \cdot (\hat{x}^{(i)}_{k+1|k} - \hat{x}_{k+1|k})^T + Q_k$
end for

1. Dynamics and Measurement Equations

There are various options in terms of modeling the dynamics of the spacecraft. The main forces acting on the spacecraft are the gravitational forces from both Didymos and Dimorphos, the solar radiation pressure (SRP), and the third body gravitation of the sun. To reduce the computational complexity, the main forces considered in this work are the gravitational attraction of the two bodies of the binary system, as shown in Eq. (7), where the subscripts D and d refer to Didymos and Dimorphos, respectively. At the distance of the DCP, it was found that for accurate modeling the point mass model is sufficient [33]. The maneuvers to change the arcs of the DCP are not added into the dynamics, as the measurements are expected to capture these as well.

$$f = -\frac{\mu_D \boldsymbol{r}_D}{r_D^3} - \frac{\mu_d \boldsymbol{r}_d}{r_d^3} \tag{7}$$

The equations of motion of the spacecraft in the TB reference frame are given as follows:

$$\ddot{\boldsymbol{r}}_H = \frac{-\mu_D \boldsymbol{r}_H}{\boldsymbol{r}_H^3} + \mu_d \left(\frac{-\boldsymbol{r}_{Hd}}{\boldsymbol{r}_{Hd}^3} - \frac{\boldsymbol{r}_d}{\boldsymbol{r}_d^3} \right) \tag{8}$$

where $\boldsymbol{r}_H$, $\boldsymbol{r}_{Hd}$, and $\boldsymbol{r}_d$ denote, respectively, the position vector of the spacecraft with respect to Didymos, the position vector of the spacecraft with respect to Dimorphos, and the position vector of Dimorphos with respect to Didymos, while μ_D and μ_d are the standard gravitational parameters of Didymos and Dimorphos.

The measurement equation correlated with the centroids' estimations is given by the pinhole camera model, which relates the three coordinates of the position x_{COM} of the COM in the TB with its two projected coordinates z_{COM} on the image plane, as shown in Eq. (9) [34].

$$z_{\mathrm{COM}} = K[A|t] x_{\mathrm{COM}} \tag{9}$$

where K is the calibration matrix that depends on the intrinsic properties of the AFC, and A and t are, respectively, the rotation matrix and the translation vector from TB to the camera reference frame. The rotation matrix A at each point in time is assumed to be given by the onboard attitude determination system.

The range measurement equation is the norm of the spacecraft position vector given in Eq. (10).

$$z_\rho = \sqrt{x^2 + y^2 + z^2} \tag{10}$$

Equations (9) and (10) show that both measurements involve the position estimation, which means that the velocity estimation is provided just by the dynamic equation given by Eq. (7). It can also be seen that in the camera reference frame, Eq. (9) affects the X and Y coordinates of the position estimation, while Eq. (10) affects the Z coordinate.

IV. Results

In this section, the results of the visual-based navigation algorithm for the relative state estimation of Hera with respect to Didymos during the DCP trajectory are presented. The performances of the IP on estimating the position of $\mathrm{COM_{Did}}$ and $\mathrm{COM_{Dim}}$ are presented with the absolute error with respect to the GT value, using the metric defined in Eq. (11). This metric is applied to both i and j directions of the PANGU viewer. The analysis is conducted only for the absolute error, as the presence of potential systematic error and biases toward positive or negative values of the centroiding estimation error has already been analyzed in [17].

$$\epsilon_{\mathrm{COM}} = |\mathrm{COM}_{\mathrm{GT}} - \mathrm{COM}_{\mathrm{est}}| \tag{11}$$

These results are compared with the ones shown in Table 5, presented in [17] and obtained applying the same CNN-based IP algorithm

Table 5 Centroiding results on old shape models of Didymos and Dimorphos [17]

Image axis	ϵ_{COM} Didymos, pxl	ϵ_{COM} Dimorphos, pxl
i direction	5.35	11.05
j direction	4.41	7.17

on 6052 images generated with PANGU during the ECP trajectory and showing the shape models of Didymos and Dimorphos before DART's close encounter. The results shown in Table 5 comply with the pointing accuracy requirements of the mission [11].

Figure 13 shows two sample images of Dataset 2 processed by the HRNet for the 26 keypoint regression.

The accuracy of estimating the spacecraft's range from the primary is assessed through the APE with respect to the GT value. The Hera mission requires that the MAPE on the range estimation is lower than 10% along the trajectory [10]. For the ECP, the MAPE obtained by the IP algorithm developed in this work is 2.1385%, thus satisfying the mission requirements. Finally, the results of the navigation filter on the estimated state of the DCP are presented.

The trained model is run with MATLAB on the NVIDIA GeForce RTX 2070 with Max Q-design GPU of the local machine. The average computational time required for processing a single image from the IP block is 2.4828 s with a standard deviation of 0.21 s. On an onboard spacecraft-like CPU processor such as the Zynq 7000 System-on-a-Chip, the average computational time is 165 s with a standard deviation of 0.15 s. On a CPU processor with higher performances, such as the LEON3 on-board the Hera spacecraft, half the computational time to process a single image is expected.

A. Centroiding Didymos

Figure 14 illustrates the results of the centroiding of Didymos for the DCP testing dataset of 450 images. It is possible to see that the absolute error fluctuates around 11.24 pxl in the i direction and around 5.95 pxl in the j direction, with a standard deviation of $\sigma_i = 11.63$ pxl and $\sigma_j = 6.01$ pxl. The error is greater in comparison to the old results shown in Table 5. This is due to the fact that, during the DCP, the distance from Didymos is reduced, resulting in a larger projection of Didymos on the images. This is also shown by looking at Figs. 14 and 5: the two peaks of the error in the i direction and on the j direction of ϵ_{COM} correspond to two local minima of the range.

B. Flag Dimorphos

The performance of the IP block on the detection of Dimorphos in the images is assessed with the confusion matrix shown in Table 6. It is defined as a positive class if Dimorphos is visible in the image and as a negative class vice versa.

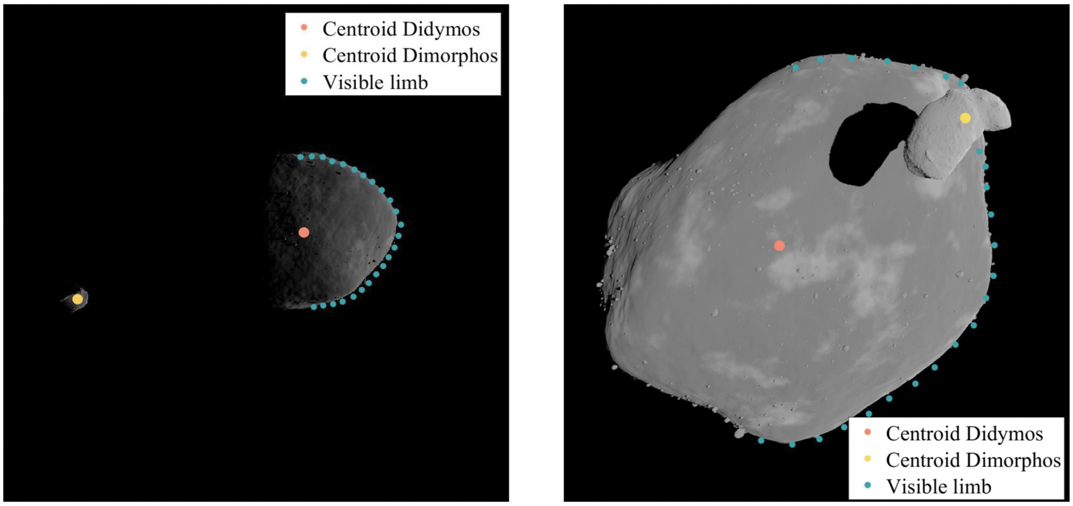

Fig. 13 Two sample images of dataset 2 with the estimated keypoints.

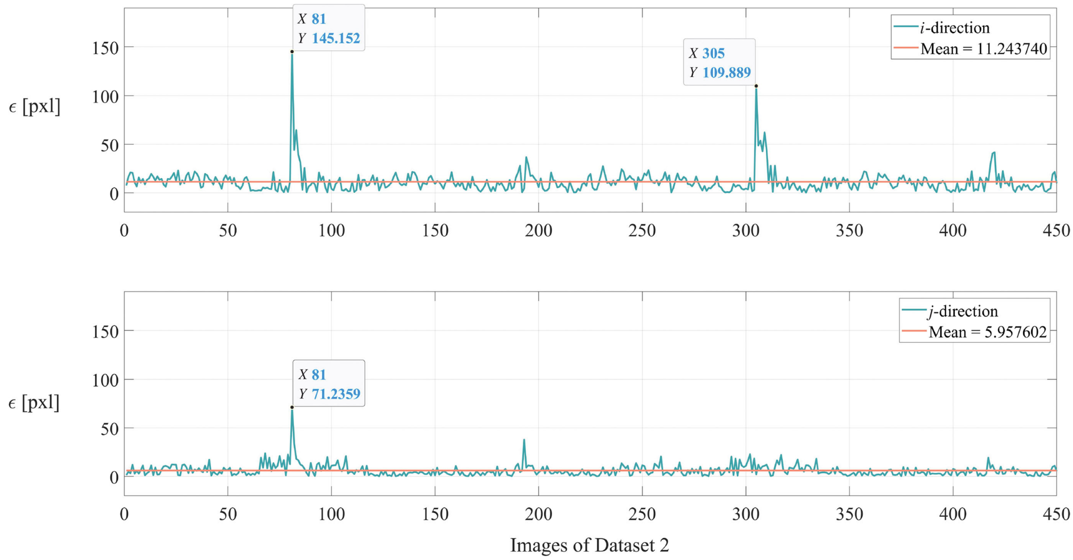

Fig. 14 ϵ_{COM} for Didymos during DCP.

Table 6 Confusion matrix detection Dimorphos

	Actual positive = 276	Actual negative = 174
Predicted positive = 247	TP = 246	FP = 1
Predicted negative = 203	FN = 29	TN = 174

Note: TP, TN, FP, and FN stand, respectively, for true positive, true negative, false positive, and false negative.

The confusion matrix allows to calculate the metrics to evaluate the performance of Dimorphos' recognition in the images:

1) Accuracy (A): overall accuracy of the algorithm

2) Precision (P): out of all the predicted positive, what percentage is truly positive

3) Recall (R): out of the all actual positive, what percentage is truly positive

The results obtained are shown in Eqs. (12–14):

$$A = \frac{\mathrm{TP} + \mathrm{TN}}{\mathrm{TP} + \mathrm{FP} + \mathrm{TN} + \mathrm{FN}} = 93.3\% \tag{12}$$

$$P = \frac{\mathrm{TP}}{\mathrm{TP} + \mathrm{FP}} = 99.6\% \tag{13}$$

$$R = \frac{\mathrm{TP}}{\mathrm{TP} + \mathrm{FN}} = 89.4\% \tag{14}$$

The IP block is capable of identifying the presence of Dimorphos with high accuracy and precision but with a medium-high recall. By lowering the cutoff value of the peak intensity of the heatmap generated by the HRNet in the regression of the COM of Dimorphos, it is possible to minimize the FN and improve the recall. Nevertheless, this might increase the FP that is important to minimize in order to limit the number of false measurements input to the navigation filter.

C. Centroiding Dimorphos

Figure 15 illustrates the performance of the IP in estimating the position of the centroid of Dimorphos for the DCP testing subset of 247 images where Dimorphos is considered as visible by the IP. It is possible to see that the absolute error fluctuates around 17.04 pxl in the i direction and around 7.8 pxl in the j direction, with a standard deviation of $\sigma_i = 31.64$ pxl and $\sigma_j = 7.42$ pxl. The peak of the absolute error is obtained because it represents the sole FP detected by the algorithm, leading to a higher average error compared to the old results shown in Table 5.

D. Range

Figure 16 shows the estimated range attained by the IP algorithm for the DCP testing dataset. The estimation is following its GT value illustrated in Fig. 5, with an APE that oscillates around a mean value of 6.23%. The error is higher compared to the one obtained with the ECP because of the lower range of the DCP trajectory and because of the less-spherical shape of Didymos used in this work. The APE is inversely proportional to the range due to the fact that the projected image of Didymos is bigger for lower ranges. As a result, the ellipsoidal shape takes on a more prominent role, and the accuracy of approximating it as a sphere diminishes. In particular, it can be seen that the peak of the APE is obtained for the same image where the ϵ_{COM} reached its peak (Fig. 14), which means that the calculated relative average distance in pixels (n_R) is inaccurate, leading to an imprecise calculation of the estimated range [Eq. (9)]. Nevertheless, the accuracy on the range estimation complies with the Hera mission requirements (APE < 10%) [10].

Figure 17 shows the distribution of the percent error of the estimated range obtained by the IP algorithm. The mean value is $\mu = -6.14\%$ and the standard deviation is $\sigma = 3.85\%$, which means that 68.27% of the percent error value is located between -10% and -2.29%. Ultimately, the range estimations are accurate and can be used for navigation purposes.

E. Estimated State

Errors of 10 km and 0.1 m/s are introduced into each coordinate of the initial estimate of the position and velocity of the spacecraft. These errors are chosen because they are relatively high compared to the GT state. This allows to analyze the capacity of the measurements in correcting the estimated trajectory even in the worst navigation scenario. The complete settings of the UKF parameters are given in Table 7. The estimated trajectory resulting from the navigation filter is shown in Fig. 18, and the errors in the estimated position are shown in Fig. 19 in the TB reference frame and in Fig. 20 in the camera reference frame. Since the focus of this study is to estimate the position with centroid and range measurements, and there is no velocity measurement available, the velocity estimate is not shown since it is not affected.

Figure 19 shows that an initial error of 10 km in the estimated position quickly decreases after incorporating the first measurement for all the three coordinates. It can be seen that the unmodeled maneuvers connecting each arc to the other do not affect the position error, which stays lower than 5 km for the whole trajectory. The

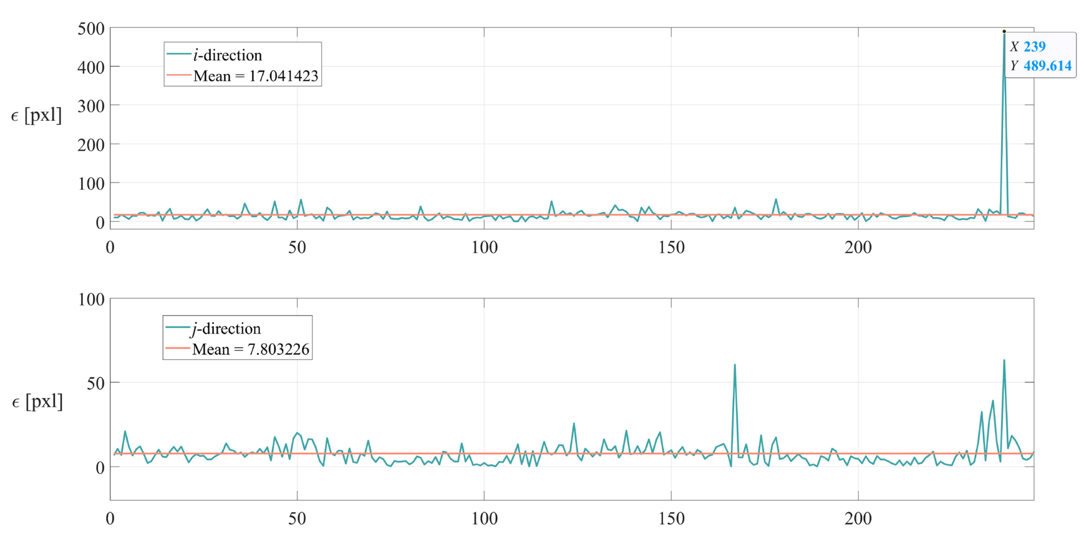

Fig. 15 ϵ_{COM} for Dimorphos during DCP.

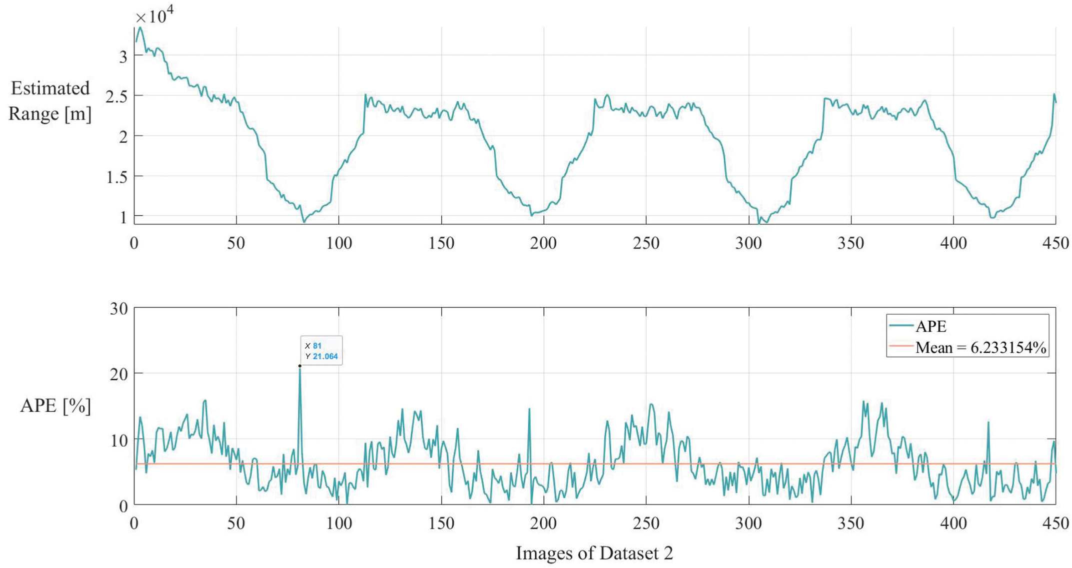

Fig. 16 Estimated range during DCP.

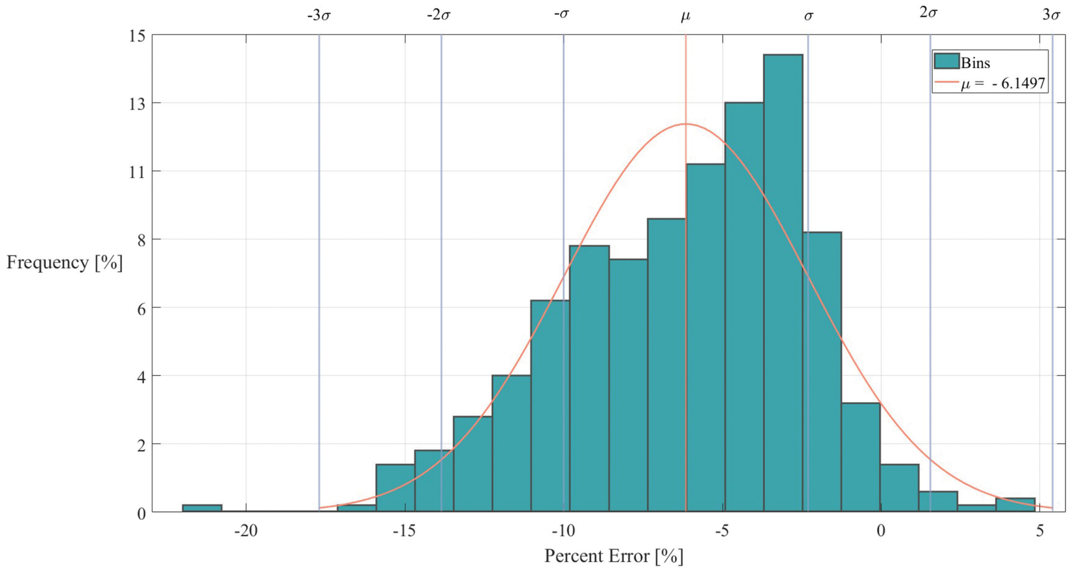

Fig. 17 Estimated range percent error distribution during DCP.

Table 7 Unscented Kalman filter variables

Variable	Symbol	Value
Initial true state	x_i	$(-1.58e4$ [m], $-2.05e04$ [m], $1.5e04$ [m], 0.0032 [m/s], 0.0138 [m/s], -0.1023 [m/s])
Initial error in position	err_p	(10, 10, 10) [km]
Initial error in velocity	err_v	(0.1, 0.1, 0.1) [m/s]
Initial covariance matrix of the state	P	(1000^2 [m], 1000^2 [m^2], 1000^2 [m^2], 0.1^2 [m^2/s^2], 0.1^2 [m^2/s^2], 0.1^2 [m^2/s]^2)
Covariance matrix of the process	Q	(1000^2 [m^2], 1000^2 [m^2], 1000^2 [m^2], 0.01^2 [m^2/s^2], 0.01^2 [m^2/s^2], 0.01^2 [m^2/s^2])
Covariance matrix of the measurements	R	Given by the IP block

appearances of local peaks are due to the fact that the attitude used in Eq. (9) presents some singularities given the particular relative geometry of the spacecraft/Sun/Didymos. This is shown more clearly in Fig. 20, where the peaks are mainly present only for the X and Y coordinates of the position estimation in the camera frame, which are the ones affected by the attitude. Therefore, a different relative geometry of the spacecraft with respect to the target would have a large impact on the general accuracy of the navigation system. Nevertheless, the developed navigation filter trained for the ECP is still able to perform well in a new environment and to generalize its solution.

V. Conclusions

In this work, an autonomous visual-based navigation technique with a CNN-based IP algorithm is developed for the DCP proximity operation of the Hera mission around the target binary asteroid system Didymos. The selected CNN architecture for this work is the HRNet. The algorithm is trained with synthetic images generated with PANGU with the previous phase of the mission, i.e., the ECP. The shape models of Didymos and Dimorphos are updated with data collected by the DART mission. The algorithm estimates the position of the centroid of Didymos and Dimorphos (if available), the range from Didymos, and the associated covariances. The covariance associated with the range estimation is selected using the results obtained with the training process. The covariance

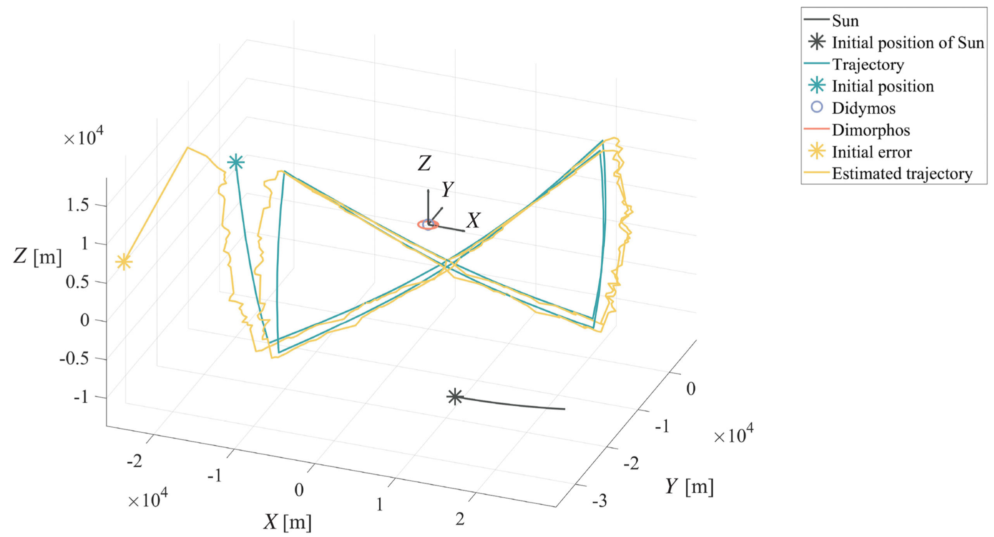

Fig. 18 Estimated trajectory vs real trajectory.

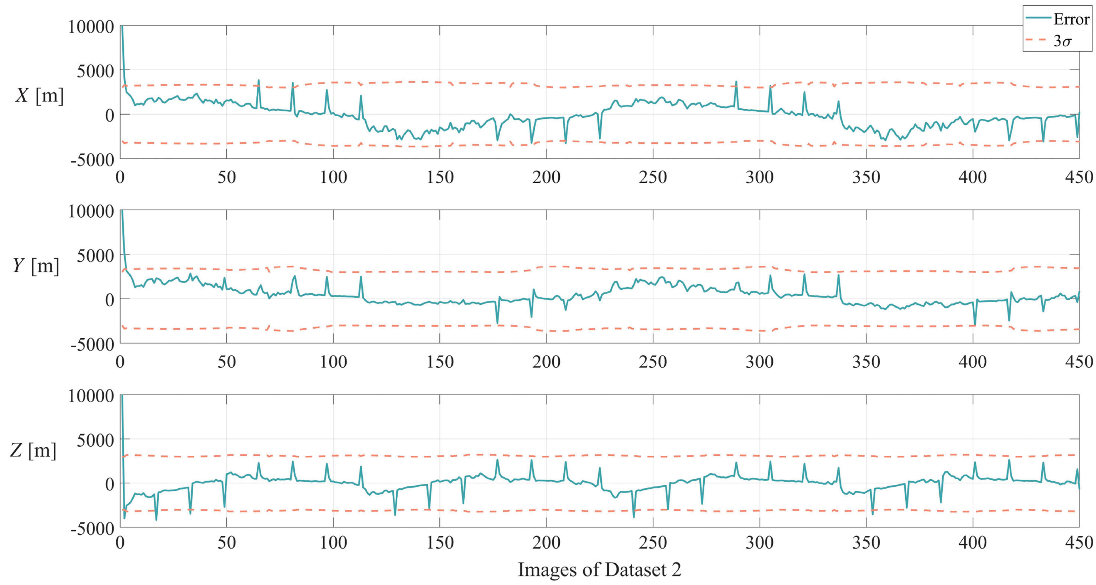

Fig. 19 Error estimated position for dataset 2 in the TB reference frame.

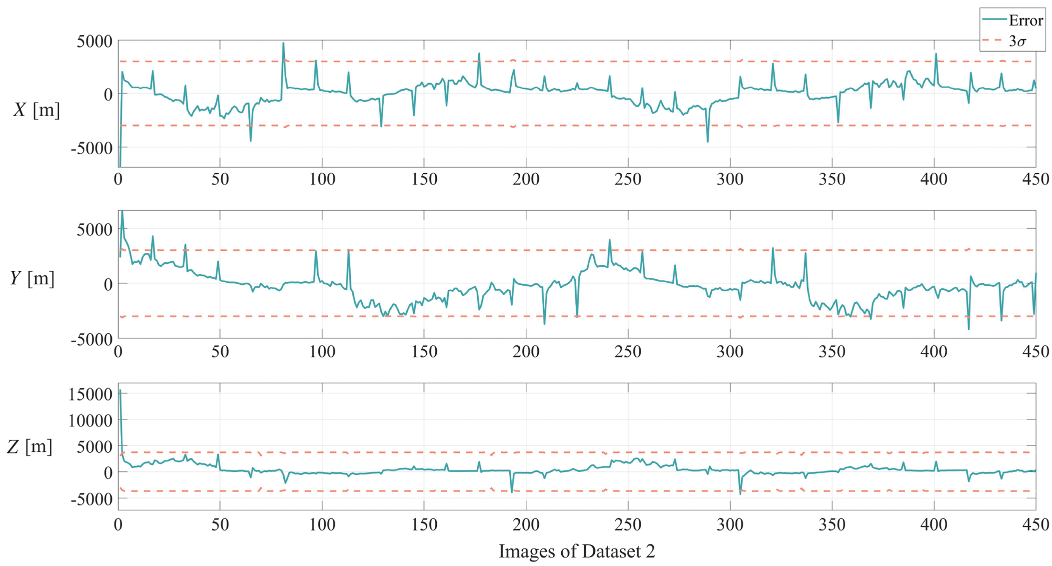

Fig. 20 Error estimated position for dataset 2 in the camera reference frame.

associated with the centroids' estimation is calculated using the heatmaps generated by the HRNet. The measurements are then combined with the dynamic environment using a UKF for the relative position estimation of the spacecraft.

The results show that the IP algorithm solves the centroiding of Didymos and Dimorphos with high accuracy independently from the ellipsoidal shape. In particular, the algorithm is able to identify whether Dimorphos is visible or not with high accuracy, precision, and recall, as shown from the confusion matrix represented in Table 6, which is a novelty of this work. The second main novelty is that the position of the centroid of Dimorphos is used by the UKF for the estimation of the state when available. The methodology to estimate the range is robust to the ellipsoidal shape of Didymos, with an error higher than the one obtained in [17], where the shape model of Didymos was more spherical. Nevertheless, the APE is lower than 10%, meeting the Hera mission requirements. The UKF is able to estimate the state of the spacecraft accurately. The source of the largest error is from the centroid estimation, which relies on the attitude of the camera reference frame even when it is singular.

The developed pipeline in this work enhances the robustness and autonomy of the navigation strategy for the Hera mission. Specifically, this work shows that it is possible to navigate around a binary asteroid system using only optical measurements. If higher accuracy for the state estimation is required, thermal or LIDAR measurements can be used. It is important to point out that if the actual shape of Didymos and Dimorphos is not the same one used in this work, an offline fine-tuning of the HRNet with a subset of images taken during the ECP is necessary to estimate the position of the centroids and the range from Didymos.

Acknowledgments

The authors would like to acknowledge the support of the Aerospace Centre of Excellence of the University of Strathclyde, United Kingdom. This study is cofunded and supported by the European Space Agency (ESA), The Netherlands, under the Open Space Innovation Platform (ESA Contract No. 4000133649/20/NL/MH/hm) and supported by GMV Defence and Space, Spain.

References

[1] Glassmeier, K. H., Boehnhardt, H., Koschny, D., Kührt, E., and Richter, I., "The Rosetta Mission: Flying Towards the Origin of the Solar System," *Space Science Reviews*, Vol. 128, Nos. 1–4, 2007, pp. 1–21. https://doi.org/10.1007/s11214-006-9140-8

[2] Yoshikawa, M., Kawaguchi, J., Fujiwara, A., and Tsuchiyama, A., "Hayabusa Sample Return Mission," *Asteroids IV*, Univ. of Arizona Press, Arizona, 2015, pp. 397–418. https://doi.org/10.2458/azu_uapress_9780816532131

[3] Watanabe, S.-i., Tsuda, Y., Yoshikawa, M., Tanaka, S., Saiki, T., and Nakazawa, S., "Hayabusa2 Mission Overview," *Space Science Reviews*, Vol. 208, Nos. 1–4, 2017, pp. 3–16. https://doi.org/10.1007/s11214-017-0377-1

[4] Lauretta, D. S., Balram-Knutson, S. S., Beshore, E., Boynton, W. V., Drouet, d'Aubigny, Enos, H. L., Golish, D. R., Hergenrother, C. W., Howell, E. S., Bennett, C. A., et al., "OSIRIS-REx: Sample Return from Asteroid (101955) Bennu," *Space Science Reviews*, Vol. 212, Nos. 1–2, 2017, pp. 925–984. https://doi.org/10.1007/s11214-017-0405-1

[5] Adams, E., Oshaughnessy, D., Reinhart, M., John, J., Congdon, E., Gallagher, D., Abel, E., Atchison, J., Fletcher, Z., Chen, M., et al., "Double Asteroid Redirection Test: The Earth Strikes Back," *IEEE Aerospace Conference Proceedings*, Inst. of Electrical and Electronics Engineers, New York, 2019, pp. 1–11. https://doi.org/10.1109/AERO.2019.8742007

[6] Michel, P., Cheng, A. F., and Küppers, M., "Asteroid Impact and Deflection Assessment (AIDA) Mission: Science Investigaation of a Binary System and Mitigation Test," *European Planetary Science Congress 2015*, Vol. 10, Nantes, France, p. 123, http://meetingorganizer.copernicus.org/EPSC2015/EPSC2015-123.pdf.

[7] "HERA Didymos Reference Model," ESA Headquarters TR 5, 2021.

[8] "Design Reference Asteroid," John Hopkins Univ. Applied Physics Lab. TR 101955, 2022.

[9] Ferrari, F., Raducan, S. D., Soldini, S., and Jutzi, M., "Ejecta Formation, Early Collisional Processes, and Dynamical Evolution After the DART Impact on Dimorphos," *Planetary Science Journal*, Vol. 3, No. 7, 2022, p. 177. https://doi.org/10.3847/PSJ/ac7cf0

[10] "HERA : Proximity Operation Guidelines," ESA-TECSAG-TN-011315, 2020.

[11] Pellacani, A., Graziano, M., Fittock, M., Gil, J., and Carnelli, I., "HERA Vision Based GNC and Autonomy," *European Conference for Aero-Space Sciences*, EUCASS, Madrid, Spain, 2019, pp. 1–14.

[12] Dias, N. G., Gordo, P., Onderwater, H., Melicio, R., and Amorim, A., "Analysis on the Isostatic Bipod Mounts for the HERA Mission LIDAR," *Applied Sciences (Switzerland)*, Vol. 12, No. 7, 2022, Paper 3497. https://doi.org/10.3390/app12073497

[13] "Mission Analysis Report," HERA-GMV-MIS-RP-00001, 2022.

[14] Pasqualetto Cassinis, L., Menicucci, A., Gill, E., Ahrns, I., and Gil-Fernández, J., "On-Ground Validation of a CNN-Based Monocular Pose Estimation System for Uncooperative Spacecraft," *8th European Conference on Space Debris*, ESA, 2021.

[15] Gil-Fernandez, J., and Ortega-Hernando, G., "Autonomous Vision-Based Navigation for Proximity Operations Around Binary Asteroids," *CEAS Space Journal*, Vol. 10, No. 2, 2018, pp. 287–294. https://doi.org/10.1007/s12567-018-0197-5

[16] Lyzhoft, J., and Wie, B., "New Image Processing Algorithm for Terminal Guidance of Multiple Kinetic-Energy Impactors for Disrupting Hazardous Asteroids," *Astrodynamics*, Vol. 3, No. 1, 2019, pp. 45–59. https://doi.org/10.1007/s42064-018-0035-x

[17] Kaluthantrige, A., Feng, J., and Gil-fernández, J., "CNN-Based Image Processing Algorithm for Autonomous Optical Navigation of Hera Mission to the Binary Asteroid Didymos," *Acta Astronautica*, Vol. 211, May 2023, pp. 60–75. https://doi.org/10.1016/j.actaastro.2023.05.029

[18] Pardo de Santanaya, R., and Lauer, M., "Optical Measurements for Rosetta Navigation Near the Comet," *International Symposium on Space Fligth Dynamics*, ISSFD, Munich, Germany, 2015, pp. 1–19.

[19] Hashimoto, T., Kubota, T., Kawaguchi, J., Uo, M., Shirakawa, K., Kominato, T., and Morita, H., "Vision-Based Guidance, Navigation, and Control of Hayabusa Spacecraft – Lessons Learned from Real Operation," *IFAC Proceedings*, Vol. 18, No. 15, 2010, pp. 259–264. https://doi.org/10.3182/20100906-5-JP-2022.00045

[20] Saiki, T., Takei, Y., Takahashi, T., Kikuchi, S., Sawada, H., Hirose, C., Terui, F., Ogawa, N., Mimasu, Y., Ono, G., et al., "Overview of Hayabusa2 Asteroid Proximity Operation Planning and Preliminary Results," *Transactions of the Japan Society for Aeronautical and Space Sciences, Aerospace Technology Japan*, Vol. 19, No. 1, 2021, pp. 52–60. https://doi.org/10.2322/tastj.19.52

[21] Williams, B., Antreasian, P., Carranza, E., Jackman, C., Leonard, J., Nelson, D., Page, B., Stanbridge, D., Wibben, D., Williams, K., et al., "OSIRIS-REx Flight Dynamics and Navigation Design," *Space Science Reviews*, Vol. 214, No. 4, 2018, pp. 1–43. https://doi.org/10.1007/s11214-018-0501-x

[22] Smith, E., Zhan, S., Adams, E., Chen, M., Bekker, D., Carrelli, D., Johnson, A., Heistand, C., Thomas, J., Badger, A., et al., "Testing Early and Often: End-to-End Testing on the Double Asteroid Redirection Test (DART)," *IEEE Aerospace Conference Proceedings*, Inst. of Electrical and Electronics Engineers, New York, 2020, pp. 1–9. https://doi.org/10.1109/AERO47225.2020.9172455

[23] Agrusa, H. F., Gkolias, I., Tsiganis, K., Richardson, D. C., Meyer, A. J., Scheeres, D. J., Ćuk, M., Jacobson, S. A., Michel, P., Karatekin, Ö., et al., "The Excited Spin State of Dimorphos Resulting from the DART Impact," *Icarus*, Vol. 370, Dec. 2021, Paper 114624. https://doi.org/10.1016/j.icarus.2021.114624

[24] "JPL Small-Body Database Browser," Jet Propulsion Lab., 2021, =https://ssd.jpl.nasa.gov/sbdb.cgi?sstr=Didymos.

[25] Naidu, S. P., Benner, L. A. M., Brozovic, M., Nolan, M. C., Ostro, S. J., Margot, J. L., Giorgini, D., Hirabayashi, T., Scheeres, D. J., Pravec, P., Scheirich, P., et al., "Radar Observations and a Physical Model of Binary Near-Earth Asteroid 65803 Didymos, Target of the DART Mission," *Icarus*, Vol. 348, Sept. 2020, Paper 113777. https://doi.org/10.1016/j.icarus.2020.113777

[26] "Hera Mission Instruments," European Space Agency, 2021, https://www.heramission.space/hera-instruments.

[27] Sierks, H., Keller, H. U., Jaumann, R., Michalik, H., Behnke, T., Bubenhagen, F., Büttner, I., Carsenty, U., Christensen, U., Enge, R., et al., "The Dawn Framing Camera," *Space Science Reviews*, Vol. 163, Nos. 1–4, 2011, pp. 263–327. https://doi.org/10.1007/s11214-011-9745-4

[28] Dunstan, M., and Martin, I., "Planet and Asteroid Natural Scene Generation Utility User Manual," STAR-Dundee TR 2, 2017.

[29] Sun, K., Zhao, Y., Jiang, B., Cheng, T., Xiao, B., Liu, D., Mu, Y., Wang, X., Liu, W., and Wang, J., "High-Resolution Representations for Labeling Pixels and Regions," 2019, https://arxiv.org/abs/1904.04514.

[30] Sun, K., Xiao, B., Liu, D., and Wang, J., "Deep High-Resolution Representation Learning for Human Pose Estimation," *Proceedings of the IEEE Computer Society Conference on Computer Vision and Pattern Recognition*, Vol. 2019, Inst. of Electrical and Electronics Engineers, New York, June 2019, pp. 5686–5696. https://doi.org/10.1109/CVPR41558.2019

[31] Pasqualetto Cassinis, L., Fonod, R., Gill, E., Ahrns, I., and Gil-Fernández, J., "Evaluation of Tightly- and Loosely-Coupled Approaches in CNN-Based Pose Estimation Systems for Uncooperative Spacecraft," *Acta Astronautica*, Vol. 182, May 2021, pp. 189–202. https://doi.org/10.1016/j.actaastro.2021.01.035

[32] Julier, S. J., and Uhlmann, J. K., "Unscented Filtering and Nonlinear Estimation," Inst. of Electrical and Electronics Engineers, New York, 2004, pp. 401–402.

[33] Ferrari, F., Franzese, V., Pugliatti, M., Giordano, C., and Topputo, F., "Trajectory Options for Hera's Milani CubeSat Around (65803) Didymos," *Journal of the Astronautical Sciences*, Vol. 68, No. 4, 2021, pp. 973–994. https://doi.org/10.1007/s40295-021-00282-z

[34] Sinha, S. N., *Pan-Tilt-Zoom (PTZ) Camera*, Springer International Publ., Cham, Switzerland, 2020, pp. 1–7. https://doi.org/10.1007/978-3-030-03243-2_496-1

K. Bollino
Associate Editor